

Measurement of stopping beam distributions in the PIBETA detector

E. Frlež^{a,1}, M. Bychkov^a, W. Li^{a,b}, and D. Počanić^a

^a *Department of Physics, University of Virginia, Charlottesville, VA 22904-4714*

^b *Department of Radiation Oncology, Virginia Commonwealth University,
Richmond, VA 23298-0058*

Precise calculation of the geometrical acceptance of a large solid angle detector with an integrated stopping target relies on precise knowledge of the beam geometry. We describe four alternative methods that we used to measure the beam stopping distributions in the PIBETA detector active target: (i) light response of segmented target elements to incident beam particles, (ii) backtracking of charged particles from π^+ and μ^+ decays using multi-wire proportional chambers, (iii) volume distribution of the Dalitz decay ($\pi^0 \rightarrow \gamma e^+ e^-$) event vertices, and (iv) the opening angle distribution of two π^0 photons originating from the beta decay of π^+ at rest. We demonstrate consistent results obtained by these four independent approaches and show how particular beam stopping distributions affect the detector's geometrical acceptance.

PACS Numbers: 29.25.t, 29.40.Gx, 41.75.i, 41.85.Ew

Keywords: Stopping beam targets; Tracking and position sensitive detectors; Charged particle beams; Beam profiles

¹ Corresponding author. Tel: +1-434-924-6786; fax: +1-434-924-4576.
E-mail address: frlez@virginia.edu (E. Frlež).

1 Introduction

The PIBETA project at the Paul Scherrer Institute (PSI) is a program of measurements which aims to make a precise determination of the $\pi^+ \rightarrow \pi^0 e^+ \nu_e$ decay rate, initially with an uncertainty of $\sim 0.5\%$ [1,2]. The small branching ratio ($\simeq 1 \times 10^{-8}$) for the pion beta ($\pi\beta$) decay and the required high measurement precision impose stringent requirements on the experimental apparatus.

The experimental signature of a $\pi^+ \rightarrow \pi^0 e^+ \nu_e$ event is determined by the prompt decay $\pi^0 \rightarrow \gamma\gamma$. The detector must be able to handle high event rates and cover a large solid angle with high efficiency for π^0 detection. Efficient hardware suppression of background events requires good energy and timing resolution. At the same time the system must operate with low systematic uncertainties and be subject to accurate calibration.

We have chosen to detect $\pi\beta$ decays at rest, and to use $\pi^+ \rightarrow e^+ \nu_e$ (π_{e2}) decays for normalization of the absolute branching ratio. Consequently, our apparatus has the following main components [3]:

- (1) a forward beam counter (BC), an active degrader (AD) and a segmented active target (AT) to stop the beam pions;
- (2) two concentric cylindrical multi-wire proportional chambers (MWPC₁ and MWPC₂) surrounding the active target for charged particle tracking;
- (3) a segmented fast veto scintillation counter (PV) surrounding the MWPC's, for the particle identification;
- (4) a high resolution, 240-module, pure CsI segmented fast shower calorimeter surrounding the active target and tracking detectors in a near-spherical geometry;
- (5) cosmic ray veto counters (CV) around the entire apparatus.

The $\pi\beta$ branching ratio $B_{\pi\beta}$ is evaluated from the following expression:

$$B_{\pi\beta} = \frac{f_{\pi_{e2}} \cdot B_{\pi_{e2}}}{B_{\pi^0 \rightarrow \gamma\gamma}} \cdot \frac{N_{\pi\beta}}{N_{\pi_{e2}}} \cdot \frac{A_{\pi_{e2}}}{A_{\pi\beta}} \cdot \frac{\epsilon_{\pi_{e2}}}{\epsilon_{\pi\beta}}, \quad (1)$$

where $B_{\pi\beta}$, $B_{\pi_{e2}}$ and $B_{\pi^0 \rightarrow \gamma\gamma}$ are the branching ratios for the $\pi\beta$, $\pi^+ \rightarrow e^+ \nu_e$ and $\pi^0 \rightarrow \gamma\gamma$ processes, respectively, $N_{\pi\beta}$ and $N_{\pi_{e2}}$ represent the detected numbers of good $\pi\beta$ and $\pi^+ \rightarrow e^+ \nu_e$ events, $A_{\pi\beta}$ and $A_{\pi_{e2}}$ are the detector acceptances, $\epsilon_{\pi\beta}$ and $\epsilon_{\pi_{e2}}$ are the detector efficiencies, and $f_{\pi_{e2}}$ is the prescaling factor for the $\pi^+ \rightarrow e^+ \nu_e$ trigger.

Due to the similarities between the two classes of events, the acceptances $A_{\pi\beta}$ and $A_{\pi_{e2}}$ are nearly equal. At the same time, both are functions of

- (1) the geometrical solid angle covered by the calorimeter;
- (2) geometry of a beam stopping distribution;
- (3) energy line-shapes of photon- and positron-induced showers in the calorimeter;
- (4) software cuts imposed on the measured event variables.

The main source of uncertainty of geometrical nature in the absolute acceptance ratio $A_{\pi e2}/A_{\pi\beta}$ has to do with the position and spatial spreading of the pion beam stopping distribution. Due to the cylindrical symmetry of our detector system the uncertainties can be broken down into lateral (x - y coordinates perpendicular to the beam direction) and axial uncertainties (z coordinate in the direction of the beam axis). Of the two, the lateral uncertainties produce a larger effect on the acceptances than the axial uncertainties. Also, since the $\pi\beta$ events require symmetrical coverage for the two photons emitted in the π^0 decay (nearly at rest), $A_{\pi\beta}$ is affected more than $A_{\pi e2}$.

In this report we analyze the PIBETA data we have collected in order to monitor the centroid and shape of the pion beam stopping distribution. Our goal is to examine how the uncertainty in the deduced beam geometry affects the $A_{\pi e2}/A_{\pi\beta}$ ratio. In Section 2 we specify the design and layout of the experimental beam line. Sections 3 and 4 address the related issue of geometrical uncertainties associated with the assembly of the modular shower calorimeter. In Section 5 we describe the PIBETA detector's central region, most importantly the segmented active target. Section 6 lays out the method and specifies the accuracy with which the lateral distribution of stopping pions (and contaminating positrons) can be deduced from their respective calibrated pulse height spectra in the active target segments. Section 7 introduces an alternative way of determining the beam position and shape that relies on the back-tracking of charged particles using MWPC hits. In Section 8 the beam stopping distribution is deduced from the reconstructed vertices of the Dalitz decay events $\pi^0 \rightarrow \gamma e^+ e^-$ which originate from the pion beta decays at rest. Influence of the different beam distributions on (i) the absolute acceptance of the detector, and (ii) measured $\pi^0 \rightarrow \gamma\gamma$ opening angle distributions, is calculated in a Monte Carlo (MC) detector simulation and presented in Section 9. Finally, the mutual consistency of the beam profile reconstructions by these four independent methods is summarized in the Conclusion.

2 PIBETA detector beam line

The measurements are performed in the $\pi E1$ channel at PSI [4]. The beam line is operated in the high intensity, low momentum resolution mode. A 114

MeV/c π^+ beam tune is developed with momentum spread $\Delta p/p \leq 1.2\%$ and maximum nominal π^+ beam intensity I_π of $\simeq 1.2 \cdot 10^6 \pi^+$'s per second.

The spatial spread of the π^+ beam is restricted by a lead collimator with a 7 mm pin-hole located 3.985 m upstream of the detector center. The beam particles are first registered in a 3 mm thick plastic scintillator placed directly behind the collimator. The pions are subsequently slowed in a 40 mm long active plastic degrader and stopped in an active plastic target that is positioned in the center of the PIBETA detector. The beam line properties have been computed with TRANSPORT [5] and TURTLE [6] codes. The TURTLE momentum spectrum of π^+ 's incident on the front face of the degrader counter is shown in Fig. 1.

This specific choice of the incident beam momentum allows for the optimum pion/muon/positron separation by the time-of-flight (TOF) method. The absolute TOF's measured between the beam counter and the degrader/target detectors for the beam positrons, muons, and pions are 12.7 ns, 17.4 ns, and 20.2 ns, respectively.

The beam particle triggers are defined by a four-fold coincidence between (1) forward beam counter BC, (2) active degrader AD, (3) active target AT, and (4) the accelerator rf signal. The energy depositions of minimum-ionizing positrons in BC, AD, and AT counters are 0.6 MeV, 7.2 MeV, and 9.0 MeV, respectively. The corresponding energy deposition values for 114 MeV/c pions (with kinetic energy 40 MeV) are 0.7 MeV, 13.0 MeV, and 28.0 MeV, respectively. By appropriately adjusting the discriminator thresholds and time delays of the logic signals that make up the quad coincidence, the “ π -in-beam” and “ e -in-beam” triggers, which preferentially select beam pions and positrons, respectively, are set up. A digital oscilloscope snap-shot of four trigger-defining signals at the input of the “ π -in-beam” coincidence unit is shown in Fig. 2.

The e^+ and μ^+ beam contaminations in the “ π -in-beam” trigger measured in the TOF spectra are small, $\simeq 0.4\%$ and $\simeq 0.2\%$, respectively.

3 Design and Assembly of the CsI calorimeter sphere

The design and assembly of the CsI calorimeter directly influence the precision with which the geometry of the beam and the decay particle tracks can be determined.

The spherically shaped pure CsI calorimeter is mounted inside a forged spherical steel shell which itself is supported by a steel frame. The shell has two large

axial openings of 550 mm diameter for beam entrance and exit and 220 smaller holes distributed over its surface and aligned with the axes of the individual CsI crystals. The smaller holes were made for access to the CsI photomultiplier tubes (PMT's). The beam openings were used to hold cast iron plugs with truncated pyramid shapes inside the shell to provide contact surfaces for 20 outlying shower veto crystals, respectively. These two plug plates press the stacked crystals together and hold them in place. The plugs have a cylindrical bore-hole (diameter 270 mm) for the beam which also allows access to the interior of the CsI sphere, e.g. the wire chambers, the target counters, etc.

Assembly of the calorimeter, weighing approximately 1,500 kg, proceeded as follows:

The empty spherical shell with its axis turned vertical, supported by its steel frame, was equipped with a single plug insert from below. The beam hole of this plug was used to hold a micrometer gauge with a touch-ball in place. This device allowed the measurement of a crystals' front surface distance to the center of the sphere with $100\text{ }\mu\text{m}$ accuracy. Afterwards, the whole frame was turned with the plug at the bottom. Through the other beam hole, on top now and not yet closed with its plug, all crystals already equipped with their PMT's were moved into the interior of the spherical shell. First came 10 pieces of trapezohedron-shaped veto crystals which were positioned on the flat surfaces of the upstanding pentagonal pyramid of the bottom plug. The correct distance to the center of the sphere was adjusted using threaded bolts mounted on the plug and supporting the crystals' rear end.

After all 10 bottom veto crystals were in place, the next crystal layer was stacked on top of the veto layer. Threaded tubes with bore-holes large enough to house a PMT and its mu-metal shielding were installed through the smaller holes in the shell, which are aligned with the crystals' axes. The front end of those tubes pressed against the rear surface of the crystals and thereby allowed for a precise adjustment of their distances to the detector center point, as measured with the touch-ball measurement device. Then the high voltage divider base was put through the tube and connected with the PMT. Bases for the veto crystals had to be mounted somewhat differently as there are no holes available for them on the shell due to the close proximity of the axial plugs. The closest hole, later employed for a crystal on the next layer, was used to move the veto crystals base into the sphere, then sideways until connection the the veto's PMT was possible. Small supporting structures were mounted to press the base gently against the PMT to prevent loosening due to gravity's pull for vertically mounted crystals.

When the sphere was half filled with crystals the procedure had to be changed somewhat as the upper surface of completed layers became steeper and steeper. In order to prevent the crystals from sliding down towards the sphere's center,

the measurement device at the center was replaced by a pin-holder with a pin for each crystal still to be inserted and already adjusted in length to give the correct distance of 260 mm to the center.

After the last layer of 10 veto crystals was filled in, the second pentagonally shaped plug was mounted on top and pressed against the crystal ball underneath. Calculations made prior to the assembly told us that pressing the plug by 10 mm against the crystal ball would be needed in order to pack all crystals tightly. This prediction turned out to be exactly fulfilled, giving us confidence in the correct positioning of all modules. The completed setup was turned around several times and watched for stability before the pin-holder at the center was disassembled through the beam entry/exit holes.

The detector geometry and location has been measured by the PSI surveying group using a theodolite. The upstream and downstream detector side are levelled, with the center 1506.0 ± 0.3 mm above the floor, the value corresponding to the nominal beam height in the π E1 channel. The measurement of the detector center was reproducible and the alignment of the target axis along the detector longitudinal axis is confirmed with 0.3 mm uncertainty.

4 Alignment of the MWPC's and the CsI calorimeter

Two out of the four reconstruction methods described in this paper depend on the information provided by two independent detectors, namely the readings of the MWPC's and the signals from the CsI calorimeter. Great care was taken in the proper assembly and positioning of these two detectors as already described in the previous section. During data acquisition, however, wire chambers required several maintenance sessions and they were once removed from the entire assembly and then reinserted. This could have introduced different displacements between the wire chamber centers and the center of the CsI sphere. Such a displacement could significantly affect both the reconstruction of the beam's stopping distribution as well as the measured $\pi^0 \rightarrow \gamma\gamma$ opening angle distribution. The following section describes how we ascertained the relative offsets between the centers of the calorimeter and the wire chamber coordinate systems.

On a single event basis it is not possible to find the exact initial point of interaction between a positron/photon and the face of the calorimeter relying only on the calorimeter signals. We can, however, determine whether a particular CsI detector was close to a given track. Assuming that in such a case most of the energy was deposited in the intersecting crystal, we can adopt the following procedure. We accept events with a single charged particle (e.g. $\mu \rightarrow e\nu_e\bar{\nu}_\mu$

positron) and reconstruct the MWPC track and its intercept with the calorimeter. We then scan all the energies deposited in the calorimeter modules and find the maximum value. Calculated values of the intercept coordinates corresponding to the crystal with most energy deposited can be histogrammed. The outcome of this procedure is a set of individual crystal maps, e.g., two-dimensional plots (polar angle θ versus azimuthal angle ϕ) of a given crystal “illumination” as seen by the wire chambers. Knowing the geometry of the crystal we can predict how polar angle θ and azimuthal angle ϕ projected histograms should look and then compare them to the experimental data.

Since the inner radius of the calorimeter sphere is fixed at 260 mm we have effectively reduced our problem to a two-dimensional one. Namely, everything depends only on the spherical coordinates θ and ϕ of the crystals. We know that Michel events are uniformly distributed in solid angle. Therefore, if in θ – ϕ space our crystals were rectangular, then the probability density of hitting one particular crystal (for, say, the θ projection) would be $dA/d\theta$ (where dA is infinitesimal area of the θ – ϕ projection) and therefore would be a constant. In θ – ϕ space our crystals do not have rectangular shapes and thus probability density is not a constant.

Knowledge of the exact geometry of the crystals allows us to calculate the theoretical $dA/d\theta$ analytically. The complete derivation is presented in Ref. [7]. Our θ – ϕ plots are additionally smeared by the chamber resolution. Mathematically, it means that the $dA/d\theta$ function is convoluted by some resolution function. In Sec. 7.2 we show that appropriate MWPC response is a Gaussian convolution and therefore the trial function is

$$f(m) = \int_{-\infty}^{+\infty} \frac{dA(\theta)}{d\theta} \cdot \Gamma \cdot \exp \left[-\frac{(\theta - m)^2}{\sigma^2} \right] d\theta, \quad (2)$$

where Γ , m and σ are the parameters of the Gaussian distribution, determined in a fit.

The exact position of the crystal enters the fitting function through the analytical expression for $dA/d\theta$ as well as via the limits of integration.

Fitting this function to the measured θ projection of the crystal map gives the position of the crystal vertices as seen by the chambers. A simple geometric transformation allows us to calculate the longitudinal (z) displacement of the chambers with respect to the CsI sphere. The resulting fits for the four different types of crystals are shown as examples in Fig. 3.

The final result for a set of runs under study yields

$$\Delta z = (0.063 \pm 0.040) \text{ mm}, \quad (3)$$

thus assuring us of the very precise alignment of the MWPC's and the CsI Calorimeter.

5 PIBETA detector active target

Our regular active target is a cylindrical plastic scintillation counter with a length of 50 mm and a diameter of 40 mm. The counter is segmented into 9 elements, as shown in a cross sectional drawing of the detector's central region in Fig. 4. A central target tube with a 3.5 mm radius is surrounded with four identical quadrant segments that compose an inner ring with 15 mm outer radius. The second, outer target ring is made out of four identically sized tubular segments that are rotated by 45° with respect to the inner ring. These 9 pieces are wrapped individually in aluminized Mylar foil making them optically insulated from each other. The parts are pressed together with a rubber band and the whole assembly is wrapped with a black plastic tape. Each target element is viewed by a miniature (8 mm diameter photo-cathode) Hamamatsu R7400U photomultiplier tube via a 60 mm long, tapered acrylic light-guide and is therefore acting as an independent counter. A photograph of the partially assembled target detector is presented in Fig. 5.

The analog signal from each of the target segments is divided by custom-made passive splitters into two branches. One side is discriminated in the time-over-threshold discriminator (CAMAC PS7106); its outputs are digitized in a Time-to-Digital Converter (FASTBUS LCR1877 TDC), as well as counted in a scaler unit (CAMAC PS7132H) that is read out every 10 s. The second branch is connected to an Analog-to-Digital Converter (FASTBUS LCR1882F ADC), which is gated with a 100 ns event trigger gate.

High voltages of the target segments' PMTs are adjusted using a 4.1 MeV $\pi^+ \rightarrow \mu^+ \nu_\mu$ stopping muon line as a reference until the 9 detector gains are matched when viewed on a digital oscilloscope. The final gain adjustment is done off-line using the ADC spectrum of stopping pions (see the next Section).

The five central target detectors by design receive practically the entire stopped π^+ beam, each counting at a comparable rate. The counting asymmetry (left-right or up-down) causes a shift of the centroid, that leads to a change in the integrated detector acceptance ratio. This is an easily measurable asymmetry even after the Poisson corrections for unresolved double hits and accidental coincidences with Michel decays.

6 Beam profile from active target ADC spectra

The analysis presented in this Section is based on the PIBETA data collected in 50 successive production runs, corresponding to about 2 days of uninterrupted data taking at the nominal π^+ stopping rate of $\simeq 5 \cdot 10^5 \text{ s}^{-1}$.

Two sets of ADC histograms for each of our two beam triggers are defined for 9 individual target segments. These histograms are filled off-line with an additional requirement that no particle showers are detected in the CsI calorimeter, thus suppressing hadronic interaction events and delayed weak π^+ or μ^+ decays with a final state positron, either of which could affect the target energy depositions.

Representative energy spectra for one target piece (No. 1) are shown in Fig. 6. The events in which the stopping pion (or thru-going positron) deposits its full energy in this target element are clearly distinguished in the high-energy peak. The energy spectra of all 9 target elements are empirically well represented by Gaussian distributions with square-root function tails:

$$f(E) = p_1 \exp \left[-\frac{1}{2} \left(\frac{E - p_2}{p_3} \right)^2 \right] + \theta(p_4 - p_5 E) \sqrt{p_4 - p_5 E}, \quad (4)$$

where p_i are the 5 free parameters of the fit. The events with the stopping particle sharing energy between two or more target segments due to scattering and/or beam spreading fall into a low energy tail. The low energy tail is also populated by positrons from weak pion and muon decays which miss the calorimeter. The peak-to-tail amplitude ratio depends on the pion stopping rate, the ADC gate width, as well as on the divergence of the beam at the front face of the target. The comparison of the data with the target energy depositions calculated with GEANT3 Monte Carlo [8] suggests that the beam divergence p_r/p_z is small, $\simeq 1\%$ (see also Sec. 8).

We have extracted the total number of pions and positrons stopping in each target segment by fitting their high-end energy spectra with Gaussian functions, integrating the fitted peaks and normalizing the integrals to the Monte Carlo predictions. The results are summarized in Fig. 7. The top panel shows the target counting rates for the “ π -in-beam” trigger, while the bottom diagram corresponds to the “ e -in-beam” events. The standard deviations shown are calculated from the uncertainties of the fitted Gaussian parameters and reflect both the event statistics and the quality of the fits. The central segment and the inner ring π^+ counting rates are determined with an accuracy better than 1%. The outer ring segments count the tails of the beam distribution with a 3–5% uncertainty.

We have examined the resulting target counting rates by simulating the target's response to the variety of lateral stopping beam distributions with the help of a simple Monte Carlo (MC) integration program. Good agreement between the Monte Carlo simulation and the measured rates is achieved by approximating the 3-dimensional beam profile with three separate Gaussian distributions in the three orthogonal variables x (beam left), y (up), and z (beam downstream):

$$f(x, y, z) = N_0 \left\{ \theta(x_0 - x) \cdot \exp \left[-\frac{1}{2} \left(\frac{x - x_0}{\sigma_{xL}} \right)^2 \right] + \theta(x - x_0) \cdot \exp \left[-\frac{1}{2} \left(\frac{x - x_0}{\sigma_{xR}} \right)^2 \right] \right\} \exp \left[-\frac{1}{2} \left(\frac{y - y_0}{\sigma_y} \right)^2 \right] \cdot \exp \left[-\frac{1}{2} \left(\frac{z - z_0}{\sigma_z} \right)^2 \right], \quad (5)$$

where the function $\theta(x) = 0$ for $x > 0$ and $\theta(x) = 1$ for $x < 0$, σ_{xL} and σ_{xR} are standard deviations of the horizontal x beam profile beam left (B_L) and beam right (B_R), σ_y and σ_z are beam widths in the vertical (y) and axial (z) projections, and the beam spot is centered at the point (x_0, y_0, z_0) . The asymmetry in the horizontal (x) beam profile is caused by a 4 mm thick carbon degrader inserted in the middle of the $\pi E1$ beam-line. The momentum-analyzed pions and positrons have different energy losses in the carbon absorber, and are therefore spatially separated in the horizontal plane. The passive lead collimator in front of the PIBETA detector then blocks out most e^+ 's and μ^+ 's, minimizing the non-pionic beam contamination.

All other attempted descriptions of the relative counting rates (e.g., a Lorentzian, piecewise parabolic functions, a box spectrum with or without exponential tails, etc.) resulted in far worse fits of the data.

The five parameters of the $f(x, y)$ distribution, namely σ_{xL} , σ_{xR} , σ_y , x_0 , and y_0 are calculated using the MINUIT minimization code [9] by requiring the best agreement between the distribution (2) and the data in Fig. 7 (minimum χ^2). The SEEK and SIMPLEX search methods are used to suppress the dependence of the convergence on the uncertainty of the Monte Carlo integration. SEEK minimizes the function using the Metropolis algorithm by selecting random values of the variable parameters, chosen uniformly over a hypercube centered at the best current value. SIMPLEX is a genuine multidimensional function minimization routine robust even to gross fluctuations in the function value. Both algorithms converged to the same solution.

The best parameter values obtained in the fits are summarized in the second column of Table 1. The corresponding two-dimensional distribution is shown in Fig. 8, where it is superimposed on the sub-division of our target. The

agreement between the measured counting rates and the simulated rates is within one standard deviation, with the χ^2 per degree of freedom of 0.9.

7 π^+ beam profile from back-tracking tomography

7.1 *Longitudinal π^+ stopping distribution*

The thicknesses of the beam-defining detectors, namely of the forward beam counter, the active degrader and the active target, were chosen to make the 40.6 MeV incident π^+ beam particles stop close to the center of the target. Our GEANT3 Monte Carlo simulation of the longitudinal vertex distribution of decaying π^+ 's is presented in Fig. 9. The input to the Monte Carlo is the π^+ momentum spectrum in Fig. 1. A histogram of Monte Carlo z coordinates of π^+ decay vertices is a Gaussian function with a width of $\sigma_z = 1.69 \pm 0.01$ mm and a flat upstream tail integrating to 0.86 ± 0.05 % events. The z position spread originates mainly from the energy straggling of stopping pions: the momentum spread of the incident beam contributes just 0.2 mm (or 12%) to the over-all axial distribution spread. The upstream tail represents π^+ decay-in-flight events and strong interactions with detector material.

7.2 *MWPC tracking and positional resolution*

The main decay channel of π^+ 's stopped in the target is the $\pi^+ \rightarrow \mu^+ \rightarrow e^+$ decay chain:

$$\pi^+ \rightarrow \mu^+ \nu_\mu, \quad (6)$$

followed by

$$\mu^+ \rightarrow e^+ \nu_e \bar{\nu}_\mu. \quad (7)$$

The first reaction, namely the main two-particle pion decay, results in a monoenergetic μ^+ with a kinetic energy of 4.1 MeV that stops within the target detector because of its short 1.34 mm range. The muons subsequently decay, by producing so-called Michel positrons with a typical continuous β -decay energy

spectrum characterized by its 52.5 MeV ($= m_\mu/2$) end-point. A GEANT3 simulation predicts that only $\sim 0.48\%$ of the μ^+ 's escape the target before coming to a complete stop.

The suppressed π_{e2} decay mode

$$\pi^+ \rightarrow e^+ \nu_e \quad (8)$$

proceeds with the branching ratio $B_{\pi_{e2}} = 1.24 \cdot 10^{-4}$ [10] and results in a monoenergetic 69.8 MeV positron that deposits an average of 4.5 MeV in the target. All average deposited energies, particle ranges and losses calculated in simulation assume $\sigma_{x,y} \simeq 8$ mm nominal beam spot size centered on the target.

Michel positrons [Eq. (7)] and $\pi \rightarrow e\nu$ positrons [Eq. (8)] are identified in the segmented plastic veto hodoscope PV via their characteristic energy depositions and tracked in the pair of cylindrical MWPC's [11] that surround the target region. Total positron energies are measured in the CsI calorimeter where they produce fully contained showers. The particles' energy spectra in the CsI calorimeter are used to discriminate between π^+ and μ^+ decay processes. The π_{e2} positron vertices in the target therefore coincide with the π^+ stopping points. The Monte Carlo root-mean-square (rms) of the Michel vertices turns out to be merely 0.04 mm larger than the π_{e2} rms.

The directional resolution of the MWPC's has to be known before one can use back-tracking of the charged particles to find the real distribution of vertices in the target. Cosmic muon events are ideally suited for the resolution study of the MWPC's. Clean samples of cosmic muon events are collected during weekly beam-off cyclotron maintenance periods. The cosmic event trigger requires the coincidence of the cosmic muon veto counter and a CsI calorimeter signal above the "low discriminator threshold" (~ 5 MeV).

In the off-line data analysis two additional stringent software cuts are imposed: (i) CsI calorimeter energy deposition > 200 MeV, and (ii) exactly two reconstructed hits in each MWPC. These constraints effectively remove any extraneous non-cosmic muon background. We reconstruct the cosmic muon track from a pair of hits in one MWPC and calculate the intersections of that track with the other chamber. Histogrammed differences between the calculated x_c, y_c, z_c and measured intersection coordinates x_e, y_e , and z_e represent the positional resolutions of the chamber. The typical azimuthal angle resolution $\Delta\phi$ and axial coordinate resolution Δz for the MWPC₁ chamber are shown as an illustration in two panels of Fig. 10. The $\Delta\phi$ rms is 0.74° and Δz rms is 0.97 mm.

7.3 Back-tracking tomography: reconstruction algorithm

The tomography algorithm relies on the back-tracking data obtained with the MWPC's. In the off-line analyzer computer program we define an $80 \times 80 \times 80 \text{ mm}^3$ volume containing the cylindrical beam stopping target divided into elementary cubic cells of fixed size. We use initially $80 \times 80 \times 80$ elementary cells, each with a volume of 1 mm^3 . For each reconstructed π_{e2} event a positron path length inside each elementary cell that is intersected by a MWPC track is found first. The analyzer code keeps a cumulative sum of tracks' path lengths for each individual cell. The high statistics data set ensures that the cubic cell containing the most π_{e2} vertices accumulates the largest path length sum. The distribution of path lengths therefore reflects the distribution of the decaying particles' vertices originating from the different volume elements [12].

The above-described algorithm determines accurately the center position (x_0, y_0, z_0) of the x_{π^+} , y_{π^+} , and z_{π^+} distributions. While the shape of our π^+ stopping distribution can be approximated by the product of Gaussian functions (Sec. 6), the real lateral distribution is more complicated, exhibiting outlying tails.

The Monte Carlo (MC) method is then used to find the correspondence between the input track vertex distribution in the target and the output path length distribution in the elementary cells. In the first stage one has to optimize the cell size.

We generate the MC tracks from an asymmetric Gaussian input distribution (Eq. 6) uniformly into the solid angle covered by the MWPC geometry. The points at which the tracks intersect the cylindrical chambers are smeared next by the measured MWPC positional resolutions. We simulate the experimentally measured particle direction by finding the track through smeared intersection points associated with the two MWPC's. Processing the large statistics of the MC tracks obtained in this way with the tomography algorithm described above we simulate the Σx_T , Σy_T and Σz_T projections of the path length sums. The Gaussian fits to the simulated path length histograms are thus connected to the input distribution rms's. The dependence of the reconstructed width of Σy_T on the unit cell size is shown in Fig. 11. The input rms value of the vertical beam profile was 10 mm. From this study we deduce that for an optimal cell size of 0.3 mm a small correction of $\Delta\sigma_y = 0.008 \pm 0.005 \text{ mm}$ has to be applied to the extracted rms of the vertical (y) vertex distribution.

The horizontal/lateral (x) and axial (z) rms values of the vertex profiles are treated analogously and the small correction factors ($< 0.1 \text{ mm}$) corresponding to the chosen cell size are obtained. The two-dimensional "contour" plot in Fig. 12 shows the correspondence between the input vertex distribution in the horizontal coordinate x and the simulated path length histogram.

The MC tomography reconstruction is compared with the experimental data in three panels of Fig. 13. The agreement between the data points and the predicted projections is very good: by scaling the width of the input $f(x, y)$ vertex distribution and studying the changes in the resulting chi-squares we estimate the uncertainty in the extracted $\sigma_{x_{\pi^+}}$ and $\sigma_{y_{\pi^+}}$ to be ~ 0.05 mm. These results are summarized in the third column of Table 1. The details of the analysis are given in Ref. [13].

8 Pion beam profile: Dalitz event e^+e^- vertices

The selection criteria for π^0 Dalitz decay events, $\pi^0 \rightarrow e^+e^-\gamma$, were:

- (1) no in-time hits in either active collimators or in cosmic muon vetoes;
- (2) no prompt π^+ in either the forward beam counter or in the active degrader;
- (3) total calorimeter energy deposition $10 \text{ MeV} < E_C < 200 \text{ MeV}$;
- (4) at least two minimum ionizing (MI) particle tracks pointing back to the target volume, identified as e^\pm 's via energy depositions in the plastic veto and CsI calorimeter;
- (5) at least one neutral shower with $E_\gamma > 20 \text{ MeV}$ in the CsI calorimeter within $\pm 5 \text{ ns}$ of two MI tracks;
- (6) if two or more candidate e^\pm and/or γ tracks are found in a single event, the (γ, e^+, e^-) combination with the closest timing is selected.

The candidate events satisfying the conditions listed above were written into a data summary tape in the off-line data replay.

The e^+ and e^- tracks were back-projected to the target region and a pair of points, one on each track, which are closest to each other was found. The mid-point coordinates on the line connecting the closest two track points are defined as an event vertex.

Fig. 14 shows the projection of Dalitz event vertices onto the horizontal (x), vertical (y), and beam (z) axes. The extracted peak widths, defined as a beam right and beam left Gaussian fits to the vertex distributions, are entered in Table 1, fourth column.

The widths of the beam stopping distribution as well as its position are in excellent agreement with the tomography solution discussed in Sec. 7.3 above.

9 π^+ beam profile and $\pi^0 \rightarrow \gamma\gamma$ opening angle

We have developed a complete GEANT3 Monte Carlo description of the PIBETA detector that includes all major sensitive as well as passive detector components. The user code is written in a modular form in standard FORTRAN 77 and organized into over 300 subroutines and data files [14].

The lateral distribution of the $\pi\beta$ event vertices in the x - y plane in our simulation is derived from the tomographic beam spot reconstruction of Fig. 13. In the direction of the beam axis the Gaussian π^+ stopping spectrum is generated with $\sigma_z = 1.7$ mm, as shown in Fig. 9.

The MC $\pi\beta$ event generator takes into account the phase space probability, the square of the matrix element and the radiative corrections [15,16]. The GEANT3 $\pi\beta$ detector trigger relies on the response of the CsI calorimeter; it requires two coincident neutral showers above the high energy discriminator threshold (HT) of 51.5 MeV that reconstruct into a π^0 originating from the $\pi\beta$ decay at rest.

The photon directions calculated by a logarithmic weighting method of shower localization [17]. The method is motivated by the exponential fall-off of the shower's transverse energy deposition [18]. The angular direction (θ_c, ϕ_c) of a particle initiating an electromagnetic shower in the PIBETA calorimeter is found as an energy-weighted mean:

$$\theta_c = \frac{\sum_{i=0}^N \omega_i(E_i) \theta_i}{\sum_{i=0}^N \omega_i(E_i)}, \quad (9)$$

where θ_i is the polar angle of an individual CsI module, ω_i is a weighting function, and N is the number of nearest neighbors of the crystal with maximum energy deposition E_0 . The sum is over the central crystal “0” and all of its nearest neighbors and thus contains 6 to 8 terms, depending on the shape of the centrally hit module. The formula for the azimuthal angle ϕ_c is identical to that for the polar angle with the replacement $\theta_i \rightarrow \phi_i$.

The weighting function ω_i is defined by:

$$\omega_i = \max[0, a_0 + \ln(E_i) - \ln(E_{tot})], \quad (10)$$

where the best value for the constant a_0 is determined empirically to be 5.5, and E_{tot} is the total energy deposited in $N+1$ modules that define the shower cluster.

The shape and absolute integral of the pion beta decay γ - γ opening angle histogram is very sensitive to the distribution of vertices of the initial decaying π^0 's. The acceptance $A_{\pi\beta}^{\text{HT}}$ for the high discriminator threshold HT calculated in a GEANT3 Monte Carlo simulation is

$$A_{\pi\beta}^{\text{HT}} = (1 - 0.4928 \cdot 10^{-3} \cdot r_0 - 0.7365 \cdot 10^{-3} \cdot r_0^2) \times (0.5977 - 0.2350 \cdot 10^{-2} \cdot s_r - 0.5500 \cdot 10^{-3} \cdot s_r^2), \quad (11)$$

where $r_0 = \sqrt{x^2 + y^2}$ is a lateral offset of the beam center, and s_r is a lateral width (a standard deviation) of a Gaussian-shaped beam spot, where both variables are expressed in millimeters. This expression represents our main result, parameterizing the acceptance of the PIBETA detector.

Fig. 15 shows γ - γ opening-angle histograms calculated using a GEANT3 code for three different beam spot sizes (top panel) and varying axial positions of the beam center (middle panel). The figure indicates that it pays to keep the beam spot root-mean square spread s_r as small as possible, because the detector acceptance for a tight event vertex distribution is less sensitive to its shape and position. In particular, the integrated $\pi\beta$ event acceptance is relatively insensitive to the longitudinal position z_0 of the stopping point, with $A_{\pi\beta}^{\text{HT}}$ changing $<0.07\%$ for $z_0 = \pm 10$ mm, and is therefore neglected in Eq. 11.

On the other hand, the resulting $\pi\beta$ acceptance is affected considerably by the spreading and lateral offsets of the beam profiles. Using the parameterization of Eq. (11) and propagating the uncertainties of the beam spot variables r_0 and s_r we obtain the results in Table 2. At our nominal stopped π^+ beam width of $\sigma_{x,y} \simeq 8$ mm, the change in the rms value or lateral position of the beam spot by $\simeq 1$ mm affects the $\pi\beta$ acceptance by $\simeq 1.5\%$. Therefore, the experimental knowledge of the beam geometry at the sub-millimeter scale is required to accomplish the goals of the PIBETA experiment. This paper demonstrates that the required accuracy has been achieved. If absolute normalization is done with respect to the π_{e2} acceptance, the constraint on the beam geometry uncertainty is not changed significantly because in our experimental configuration $A_{\pi_{e2}}$ is almost independent of the small variations from the nominal beam model. The geometrical acceptance $A_{\pi_{e2}}$ varies less than 0.5% for r_0 , z_0 , and s_r in 0–10 mm range.

In the bottom panel of Fig. 15 we present the MC $\theta_{\gamma\gamma}$ calculation for our average beam distribution. The measured $\theta_{\gamma\gamma}$ spectrum, based on an off-line replay of 59,011 $\pi\beta$ events is represented by full markers. For data taken over such a long time period we must take into account the temporal stability of the beam distribution. The back-tracing tomography reveals that our beam spot position and its size were remarkably stable. The reconstructed lateral

(r_T) and longitudinal (z_T) centroids of the stopping distribution vary with $\text{rms}_r \simeq 0.04 \text{ mm}$ and $\text{rms}_z \simeq 0.2 \text{ mm}$, respectively, as shown in Fig. 16. The oscillations of the beam spot location and size are included in our GEANT3 event generators. After that adjustment, $\pi\beta$ data points and the MC simulation of $\theta_{\gamma\gamma}$ agree with each other within the statistical uncertainties.

10 Conclusion

Precise knowledge of the PIBETA detector acceptance for the decay products of the stopped pion beam is required for the evaluation of the absolute branching ratios of pion and muon decay processes. The geometrical acceptances of a compact detector like ours, defined with the specific cuts on the energies and angles of measured particles, depend strongly on the distribution of vertices of decaying particles. In this paper we show that we can measure position and the volume distribution of the stopped pion beam with sub-millimeter precision. The uncertainty in the 3-dimensional beam shape or position of the order of $\simeq 0.1 \text{ mm}$ then translates into $\simeq 0.12\%$ systematic uncertainty of the acceptance calculated with the GEANT3 Monte Carlo simulation. The consistency of our four different methods of extracting the pion beam stopping distribution is summarized in Table 1.

11 Acknowledgements

We thank J. Koglin who developed the TURTLE and TRANSPORT MC simulations of our beam tunes. The mechanical support of the PIBETA detector was designed and built under supervision of H. Obermeier. Z. Hochman provided valuable technical assistance throughout the detector assembly and commissioning phases. The support from the Hallendienst and many other PSI staff members is gratefully acknowledged.

This work is supported and made possible by grants from the US National Science Foundation and the Paul Scherrer Institute.

References

- [1] D. Počanić et al., A Proposal for a Precise Measurement of the $\pi^+ \rightarrow \pi^0 e^+ \nu$ Decay Rate (following PSI R-89.01) (Paul Scherrer Institute, Villigen, 1991).
- [2] D. Počanić et al., Phys. Rev. Lett. 93 (2004) 181803-1-4.
- [3] E. Frlež et al., Nucl. Instr. and Meth. A 526 (2004) 300.
- [4] PSI Users' Guide: Accelerators Facilities (Paul Scherrer Institute, Villigen PSI, 1994).
- [5] K. L. Brown, D. C. Carey, Ch. Iselin, and F. Rothacker, Transport, a Computer Program for Designing Charged Particle Beam Transport Systems, CERN Yellow Reports 73-16/80-04 (CERN, Geneva, 1973/1980).
- [6] K. L. Brown, Ch. Iselin, and D. C. Carey, Decay Turtle, CERN Yellow Report 74-2 (CERN, Geneva, 1974).
- [7] M. Bychkov, *Measurements of the Wire Chamber's Displacement*, accessible at <http://pibeta.phys.virginia.edu>.
- [8] R. Brun, F. Bruyant, M. Maire, A. C. McPherson, and P. Zancarini, GEANT 3.21 DD/EE/94-1 (CERN, Geneva, 1994).
- [9] F. James and M. Roos, MINUIT—Function Minimization and Error Analysis, CERNLIB Long Write-up D506 (CERN, Geneva, 1989).
- [10] K. Hagiwara et al., Phys. Rev. D 66 (2002) 010001. Latest WWW update accessible at <http://www-pdg.lbl.gov>.
- [11] V. V. Karpukhin, I. V. Kisel, A. S. Korenchenko, S. M. Korenchenko, N. P. Kravchuk, N. A. Kuchinsky, N. V. Khomutov, and S. Ritt, Nucl. Instr. and Meth. A 418 (1998) 306.
- [12] R. Gordon, IEEE Trans. Nucl. Sci. NS-21 (1974) 78.
- [13] W. Li, *A Precise Measurement of the $\pi^+ \rightarrow \pi^0 e^+ \nu$ Branching Ratio*, Ph. D. Thesis (University of Virginia, Charlottesville, 2004).
- [14] E. Frlež, Complete GEANT3 Description of the PIBETA Detector, accessible at URL <ftp://pibeta.phys.Virginia.EDU> under /pub/pibeta/geant, (1997).
- [15] G. Källén, Elementary Particle Physics (Addison-Wesley, Reading, 1964).
- [16] E. S. Ginsberg, Phys. Rev. 142 (1966) 1035.
- [17] T. C. Awes, F. E. Obenshain, F. Plasil, S. Saini, S. P. Sorensen, and G. R. Young, Nucl. Instr. and Meth. A 311 (1992) 130.
- [18] L. Bugge, Nucl. Instr. and Meth. A 242 (1986) 228.

Fig. 1. The momentum spectrum of the beam π^+ 's entering the active degrader/target counters calculated by the TURTLE program [6].

Fig. 2. A “ π -in-beam” trigger is defined as a four-fold coincidence between a forward beam counter (Ch. 1), an active degrader (Ch. 2), an active target (Ch. 3), and a 19.75 ns rf cyclotron signal (Ch. 4).

Fig. 3. Determination of the offsets between coordinate systems of the MWPC's and CsI calorimeter. The MWPC's track intersections with the calorimeter sphere for which four representative crystals also have the maximum energy depositions.

Fig. 4. Cross section of the PIBETA detector central region (drawn in GEANT3). Shown are the segmented active target AT, a pair of cylindrical MWPC's, and the plastic veto hodoscope array PV.

Fig. 5. A photograph of the segmented PIBETA active target. Tapered acrylic light-guides are glued to the mutually optically isolated target segments.

Fig. 6. Representative energy spectra of beam pions (π -in-beam trigger, top panel) and beam positrons (e -in-beam trigger, bottom panel) stopping in the target segment number 1. Monte Carlo GEANT3 predictions are represented by full line spectra.

Fig. 7. Integrated counting rates in 9 target segments for the π -in-beam and e -in-beam triggers, respectively. Orientation of the coordinate system and target segment labels (0–8) are also indicated.

Fig. 8. The 2-dimensional shape of the π^+ beam superimposed on an outline of the segmented target. The reconstruction is based on the target ADC spectra collected during years 1999–2001.

Fig. 9. The z -component of the π^+ stopping distribution in the active target calculated in the GEANT3 simulation using the momentum distribution in Fig. 1.

Fig. 10. The MWPC₁ directional resolutions in the azimuthal angle ϕ (top panel), and axial coordinate z (bottom panel) extracted from a sample of cosmic muon events. The data points for ϕ and z coordinates are fitted with a sum of two Gaussians, the broader one accounting for the cosmic muon scattering in the apparatus.

Fig. 11. The dependence of reconstructed vertical rms widths σ_y of the beam stopping distribution on the size of the elementary cell used in the calculation.

Fig. 12. A lookup table for determining $\sigma_{xL/R}$ (L left, R right) is calculated starting from the synthetic source distributions in the Monte Carlo. The fitted “contour” lines correspond to the values of equal σ 's.

Fig. 13. The distribution of path length sums for x (top), y (middle) and z (bottom) coordinate projections. The experimental points for back-tracked $\pi^+ \rightarrow e^+ \nu_e$ positrons are compared with the Monte Carlo simulation that uses the beam stopping profile deduced from back-tracking tomography.

Fig. 14. The horizontal (x , the top panel) and vertical (y , the middle panel) beam profiles deduced from the Dalitz event $\pi^0 \rightarrow \gamma e^+ e^-$ vertices. The axial z coordinate cut around the target center, $\Delta z = \pm 10$ mm is imposed to select the π^+ stopping distribution (the bottom panel). The agreement with the tomography solutions is very good.

Fig. 15. The γ - γ opening angle following the π^0 decay from the $\pi^+ \rightarrow \pi^0 e^+ \nu$ process as reconstructed in the PIBETA segmented calorimeter. The GEANT3 prediction for the stopping π^+ beam profiles with three different transverse widths (top panel) and three different longitudinal stopping points (middle) is shown. The bottom panel shows a comparison of the partial $\pi\beta$ events data set with the Monte Carlo prediction. The plotted uncertainties are statistical only.

Fig. 16. The spatial stability of the π^+ beam spot center during one three month data taking period. The lateral beam center location (top) and the axial beam stopping point (bottom) are reconstructed via back-tracking tomography. The reconstruction uncertainty for a single run is < 0.02 mm.

Table 1

The rms widths and centering of the π^+ beam spot in the PIBETA active stopping target deduced by four different methods: (i) using the counting rate matrix in the segmented target, (ii) via back-tracking of $\pi^+ \rightarrow \mu^+ \rightarrow e^+$ positrons with two cylindrical MWPC's, (iii) from Dalitz decay e^+e^- pair vertices, and (iv) from fits to the opening angle distribution of two $\pi^0 \rightarrow \gamma\gamma$ photons. BR/BL stands for beam right/left, BU/BD labels beam up/down directions.

| Beam profile parameters | Segmented target rates | MWPC's back-tracking | Dalitz e^+e^- vertices | $\theta_{\pi^0 \rightarrow \gamma\gamma}$ opening angle |
|----------------------------------|---------------------------|-------------------------|-----------------------------|--|
| σ_x^R (mm, BR horizontal) | 7.0 ± 0.3 | 7.04 ± 0.04 | 6.67 ± 0.37 | 7.0 ± 0.5 |
| σ_x^L (mm, BL horizontal) | 8.8 ± 0.3 | 9.50 ± 0.07 | 8.46 ± 0.75 | 9.0 ± 0.5 |
| σ_y^U (mm, BU vertical) | 7.0 ± 0.3 | 7.44 ± 0.06 | 7.25 ± 0.49 | 7.6 ± 0.5 |
| σ_y^D (mm, BD vertical) | 7.0 ± 0.3 | 7.46 ± 0.07 | 7.40 ± 0.32 | 7.6 ± 0.5 |
| σ_z (mm, axial) | — | 1.70 ± 0.03 | 1.8 ± 0.3 | 2.0 ± 0.3 |
| x_0 (mm) | -1.0 ± 0.3 | -1.92 ± 0.05 | -0.95 ± 0.70 | -1.0 ± 0.3 |
| y_0 (mm) | 0.1 ± 0.3 | -0.12 ± 0.05 | -0.31 ± 0.60 | 0.0 ± 0.3 |
| z_0 (mm) | — | 0.30 ± 0.02 | 0.43 ± 0.12 | 0.30 ± 0.1 |

Table 2

Summary of two main uncertainties connected with the size and position of a π^+ beam spot in determining the detector acceptance $A_{\pi\beta}$. Relevant geometrical variables are a lateral offset of the π^+ beam center r_0 with respect to the geometrical center of the target and a lateral rms width of the π^+ beam profile s_r . Beam spot parameters obtained from the back-tracking tomography are used.

| Source | General value (%) | Current value (%) |
|--|--|----------------------|
| $(A_{\pi\beta}^{\text{HT}})^{-1} \cdot (\partial A_{\pi\beta}^{\text{HT}} / \partial r_0) \cdot \sigma_{r_0} _{r_0=1 \text{ mm}}$ | $1.15 \cdot \sigma_{r_0} \text{ (mm)}$ | 0.06 |
| $(A_{\pi\beta}^{\text{HT}})^{-1} \cdot (\partial A_{\pi\beta}^{\text{HT}} / \partial s_r) \cdot \sigma_{s_r} _{s_r=8 \text{ mm}}$ | $1.26 \cdot \sigma_{s_r} \text{ (mm)}$ | 0.10 |

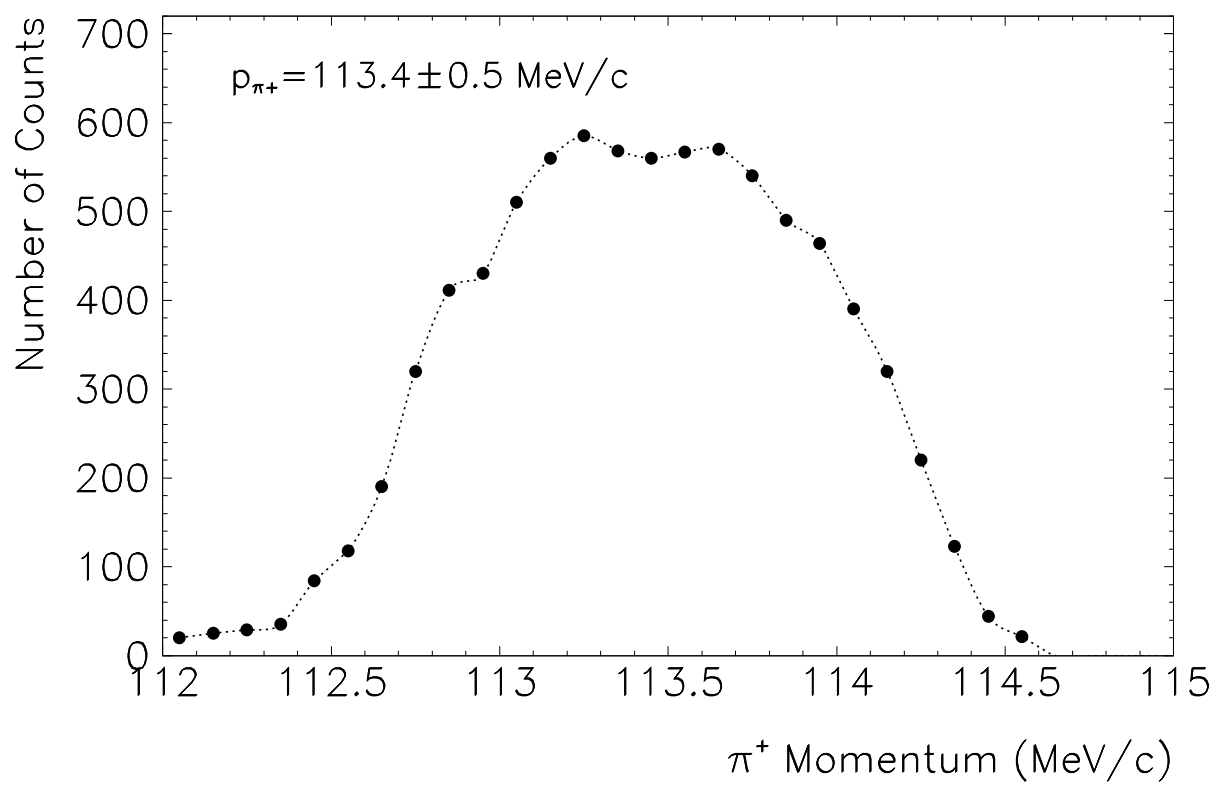


FIGURE 1

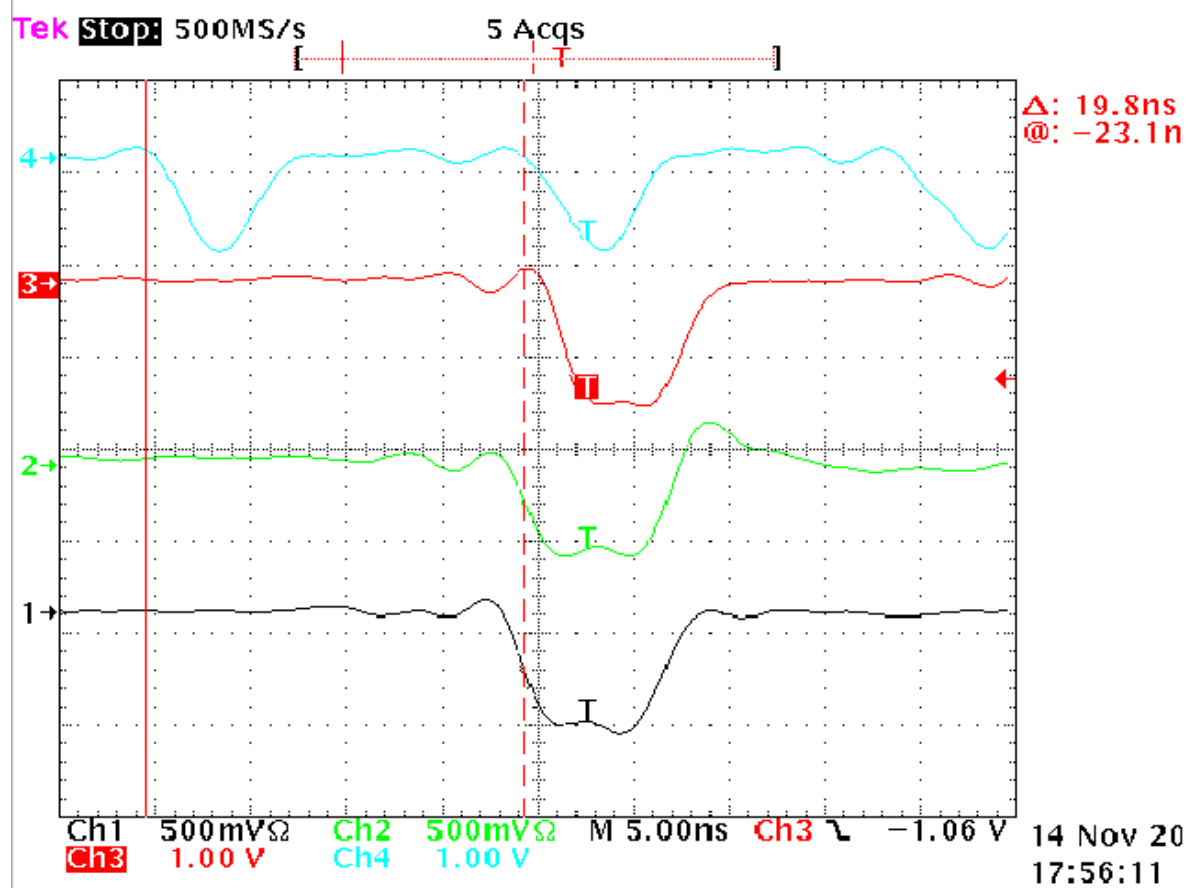


FIGURE 2

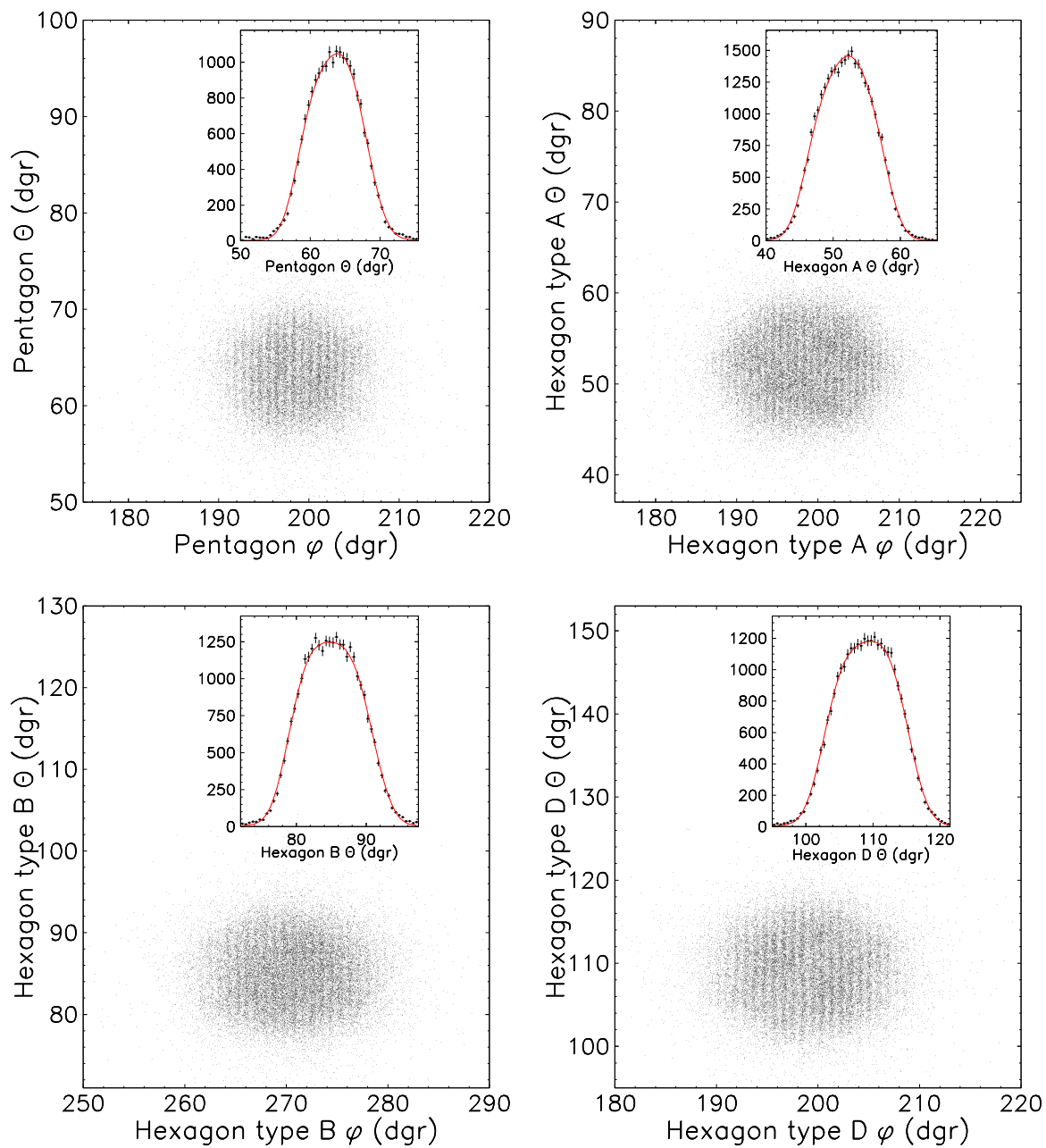


FIGURE 3

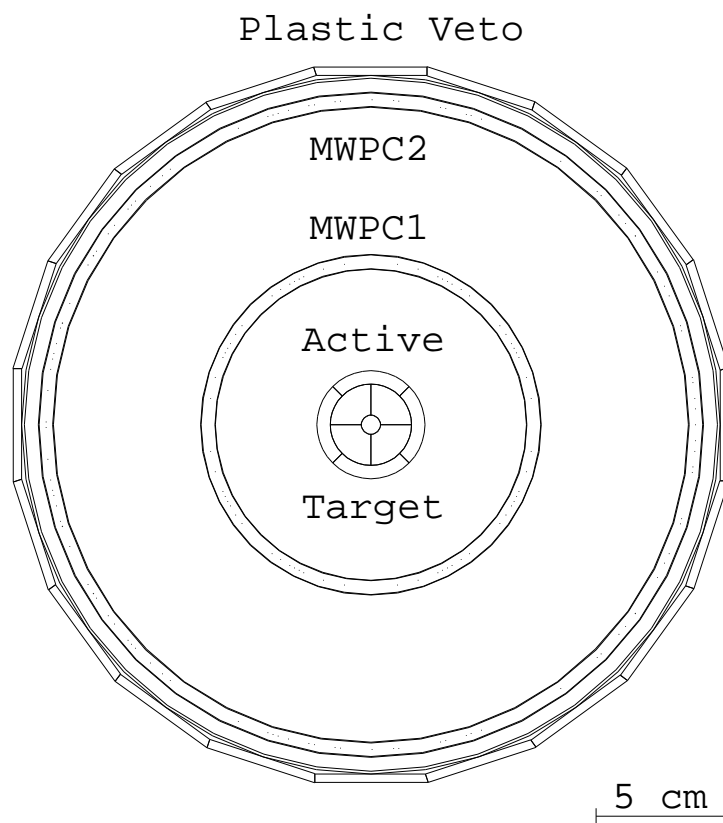


FIGURE 4

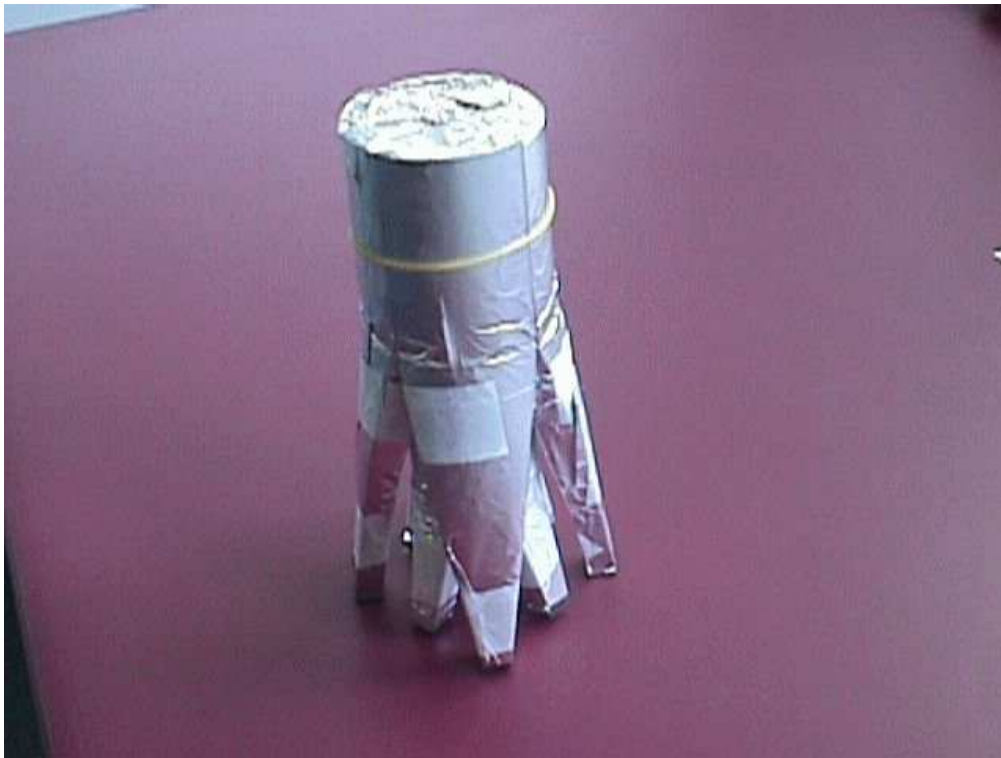


FIGURE 5

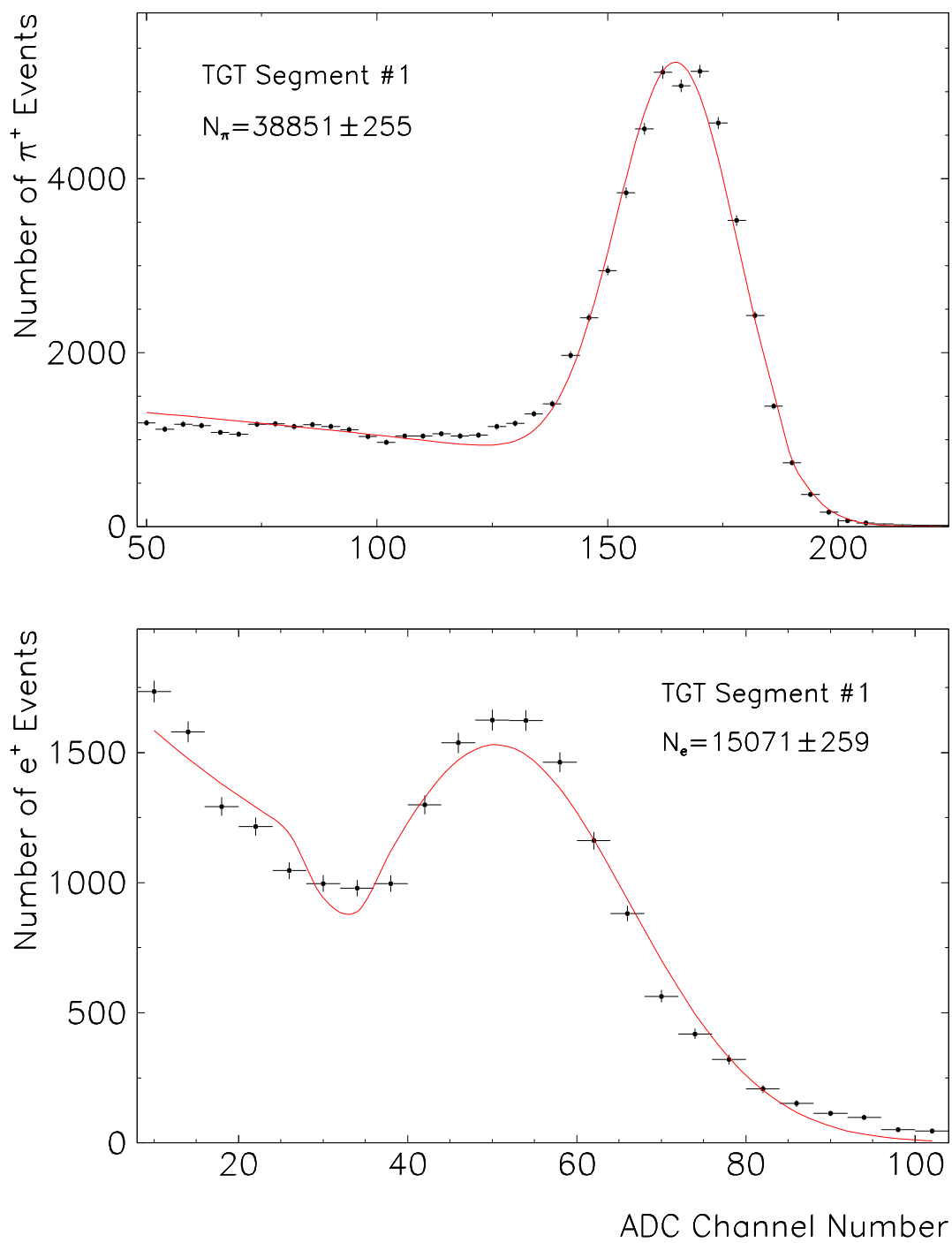


FIGURE 6

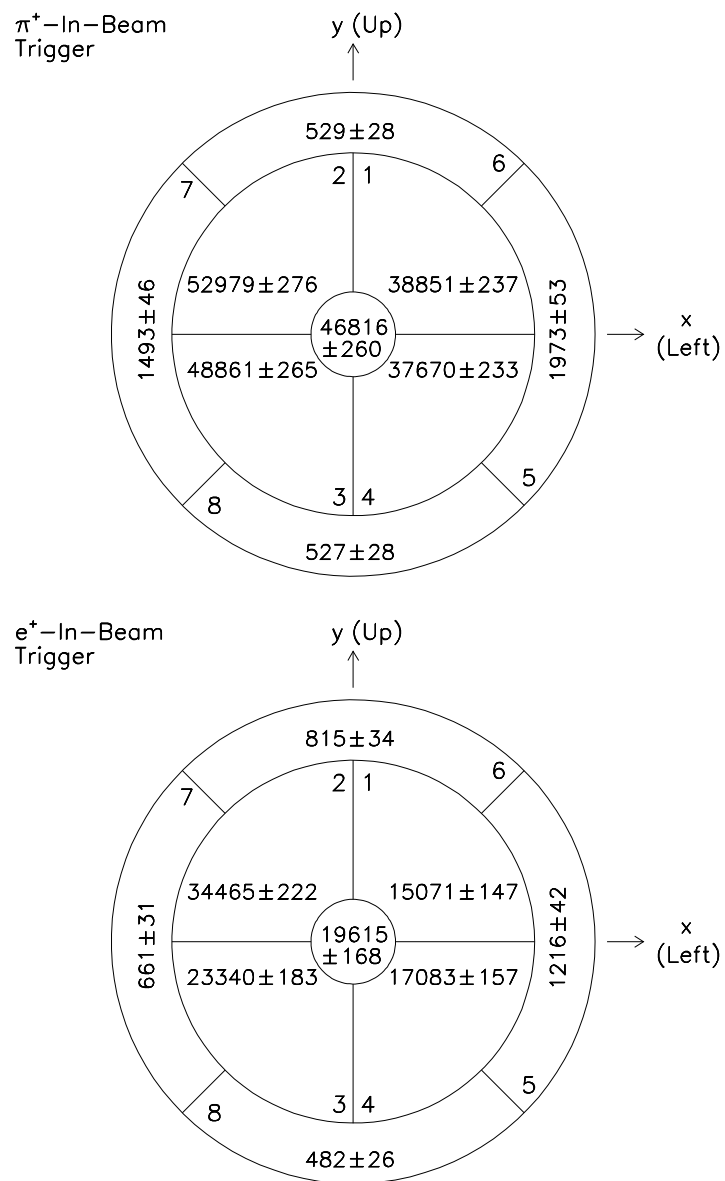


FIGURE 7

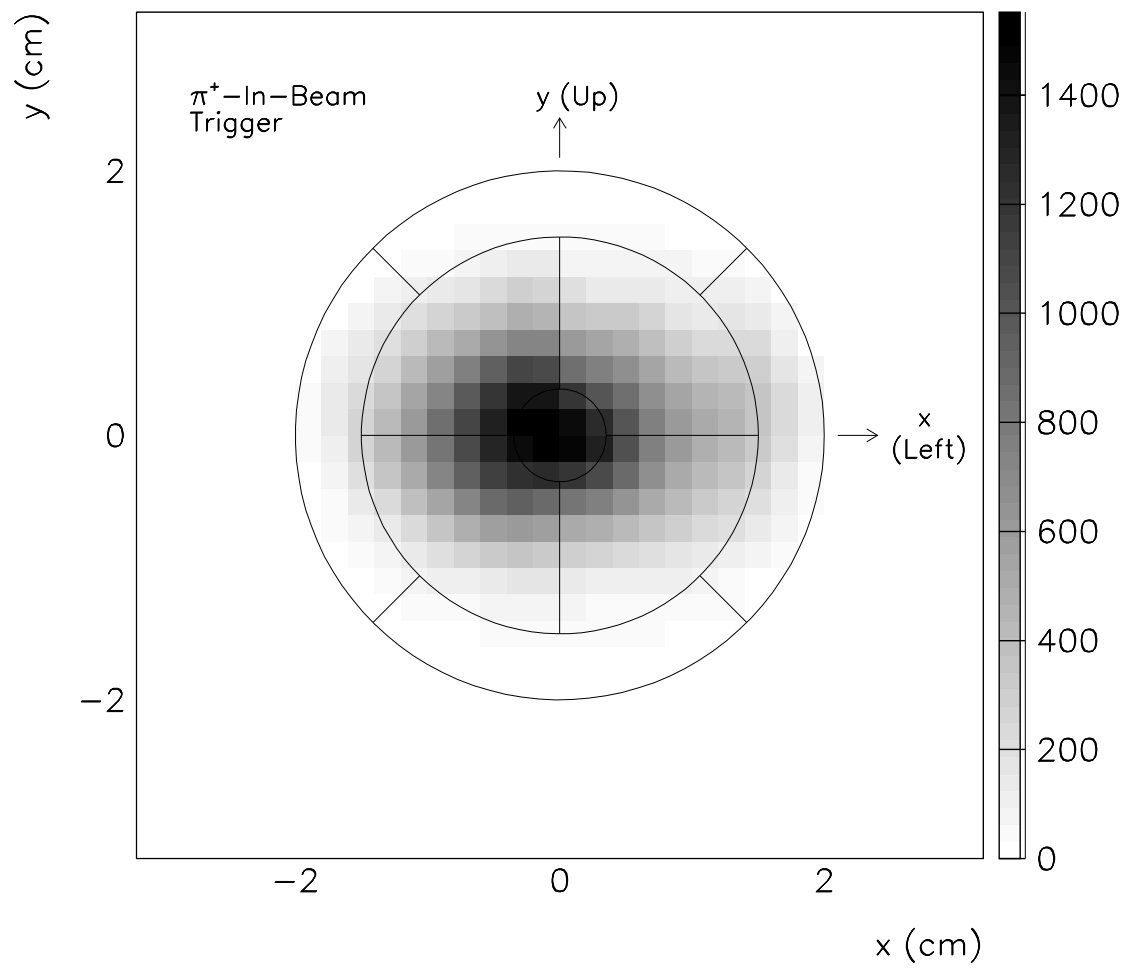


FIGURE 8

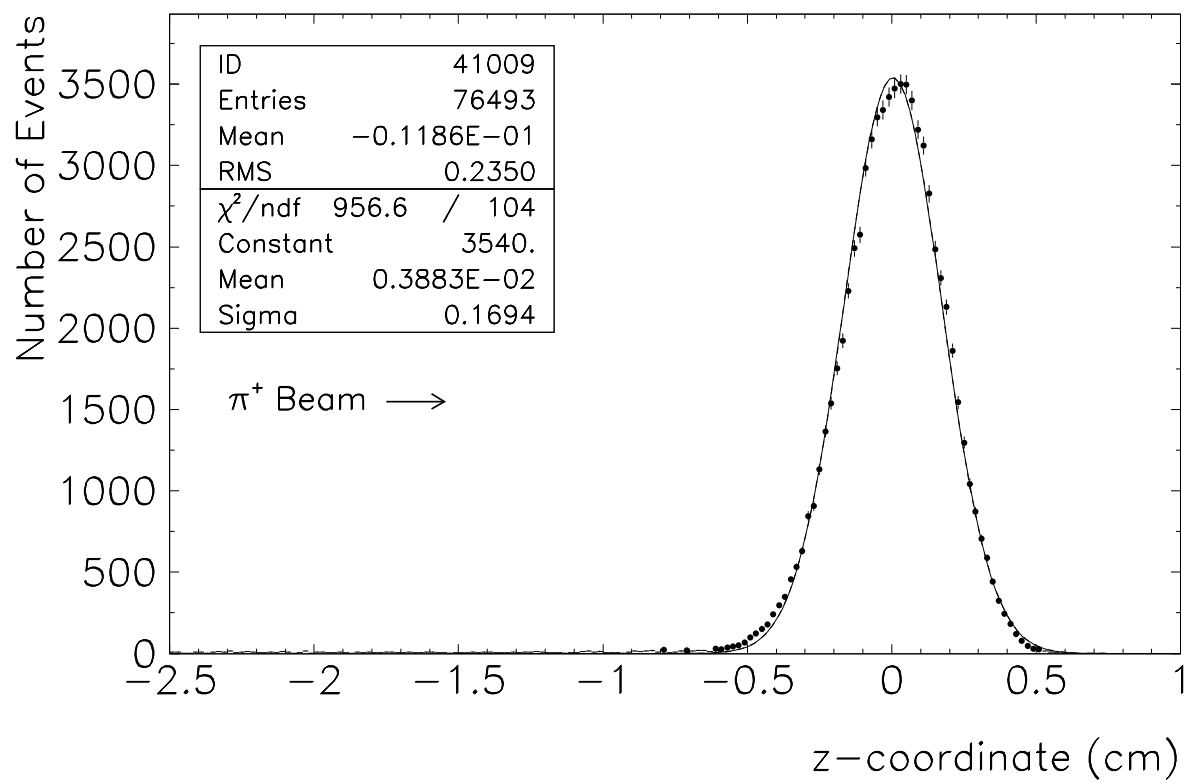


FIGURE 9

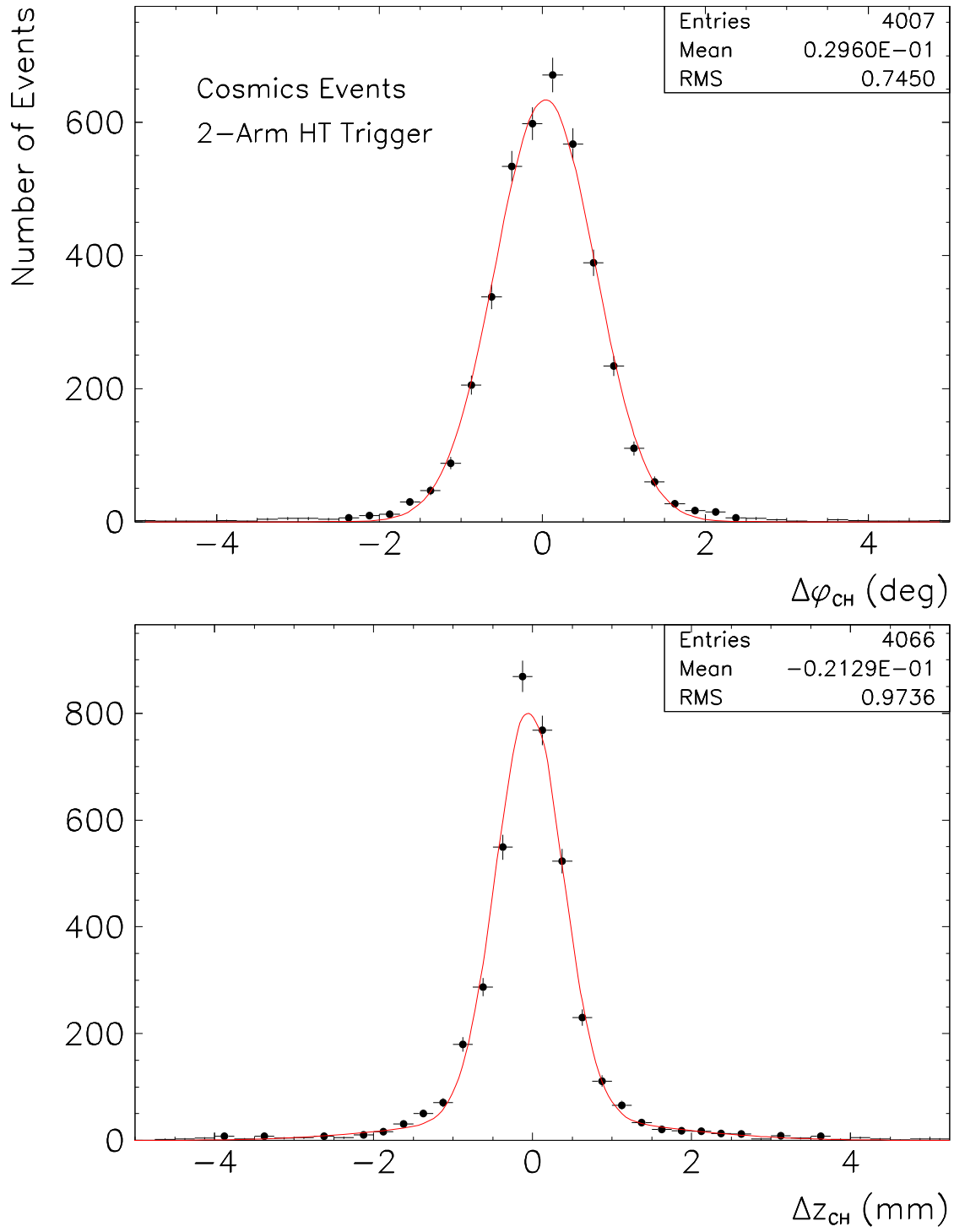


FIGURE 10

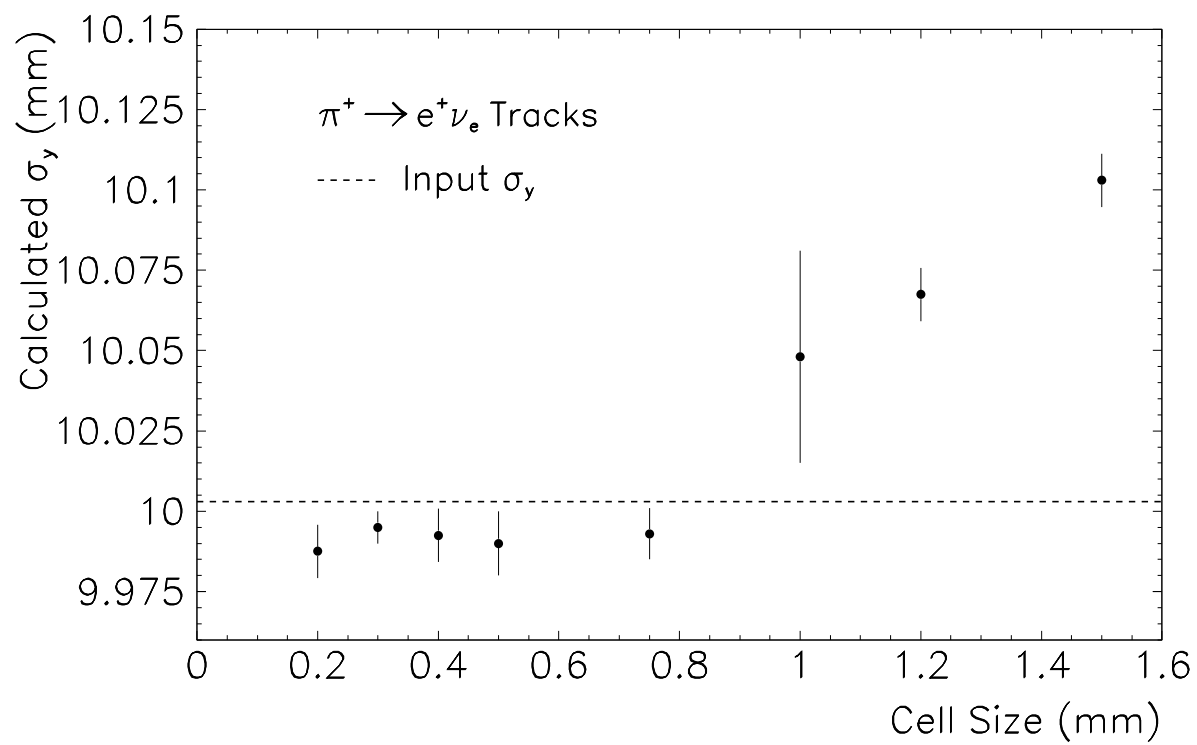


FIGURE 11

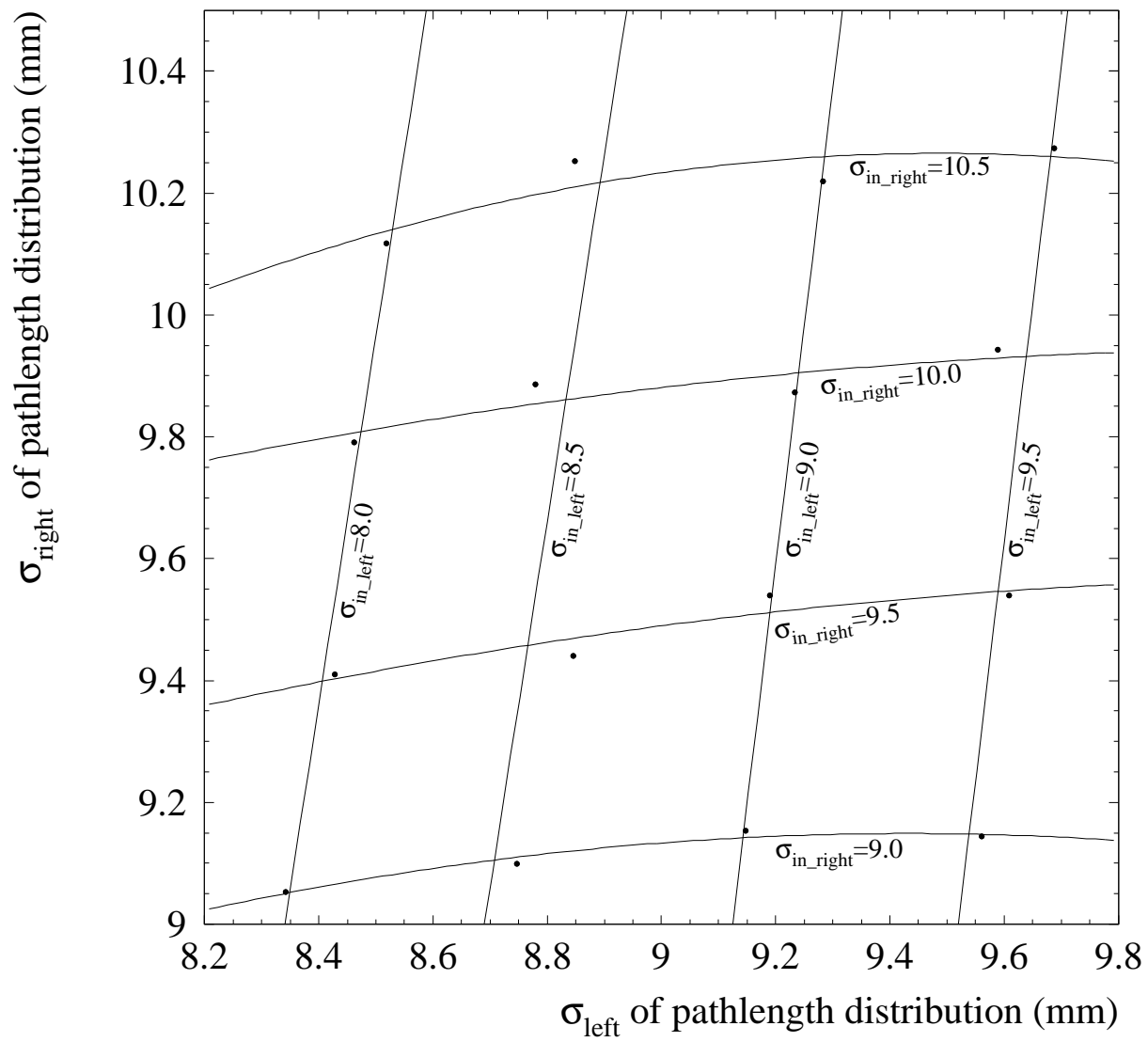


FIGURE 12

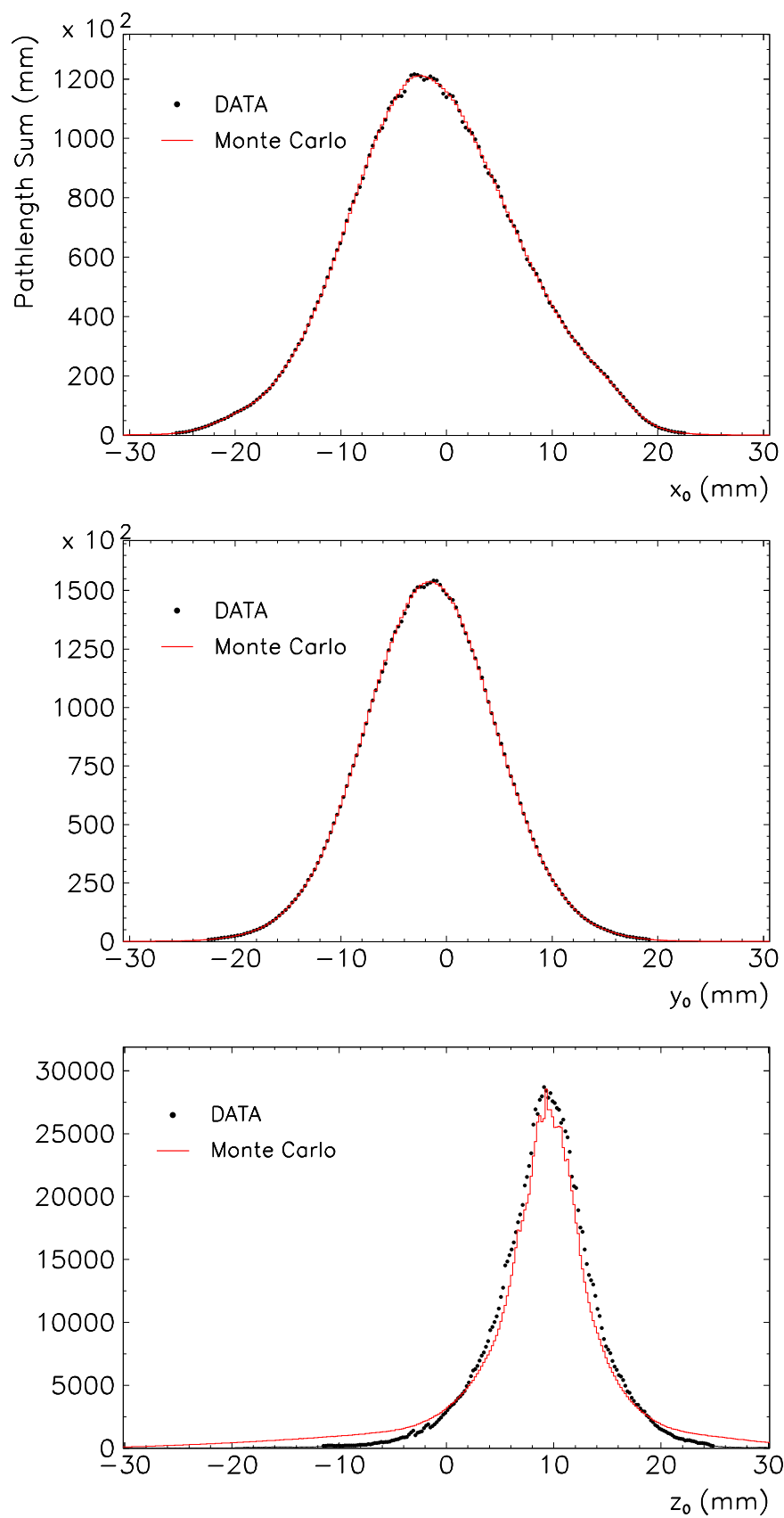


FIGURE 13

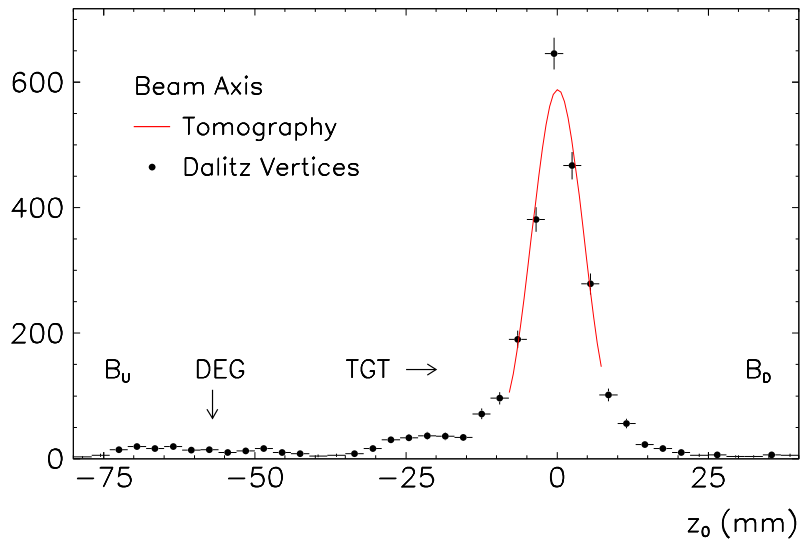
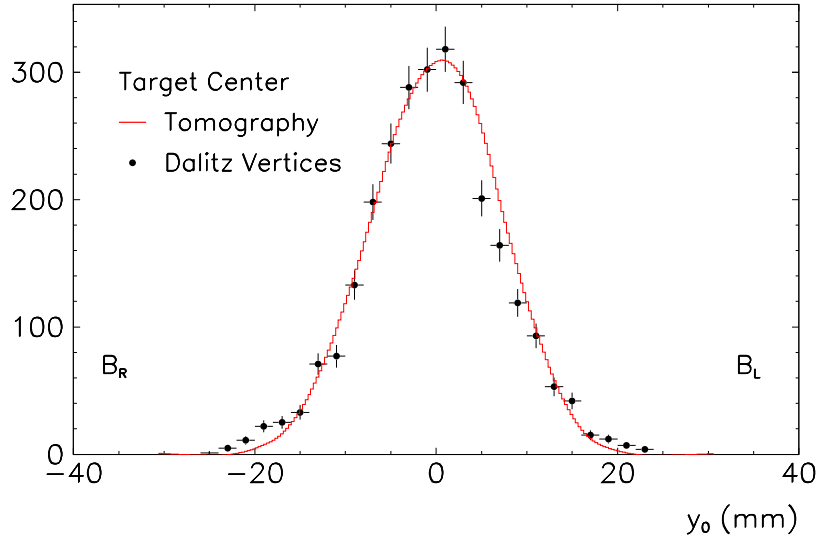
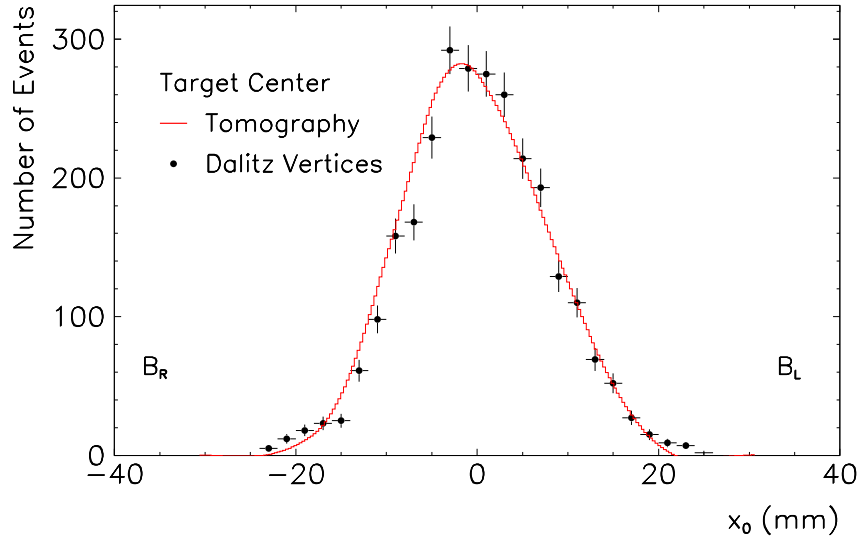


FIGURE 14

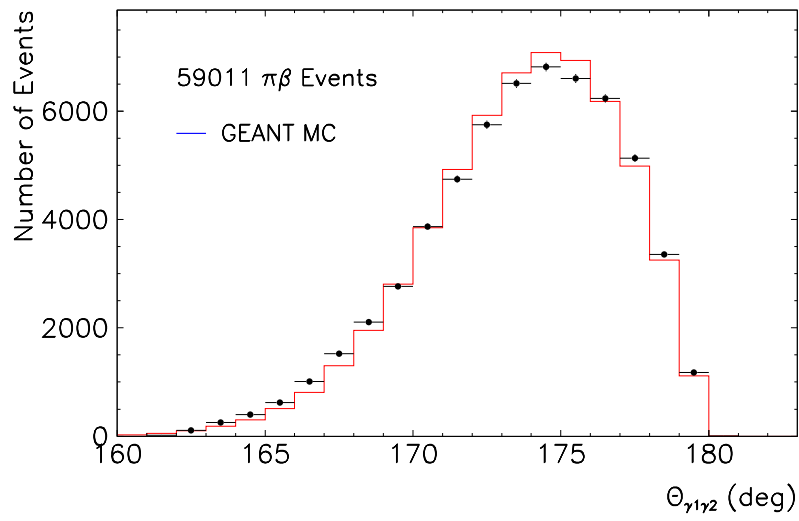
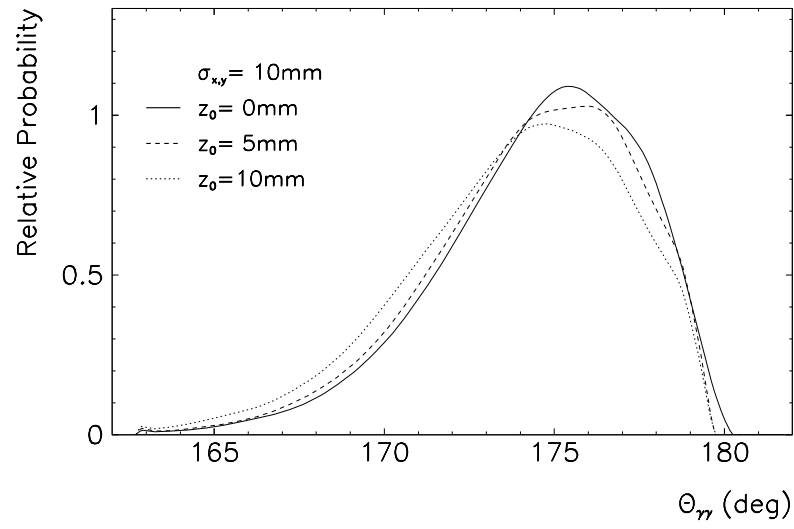
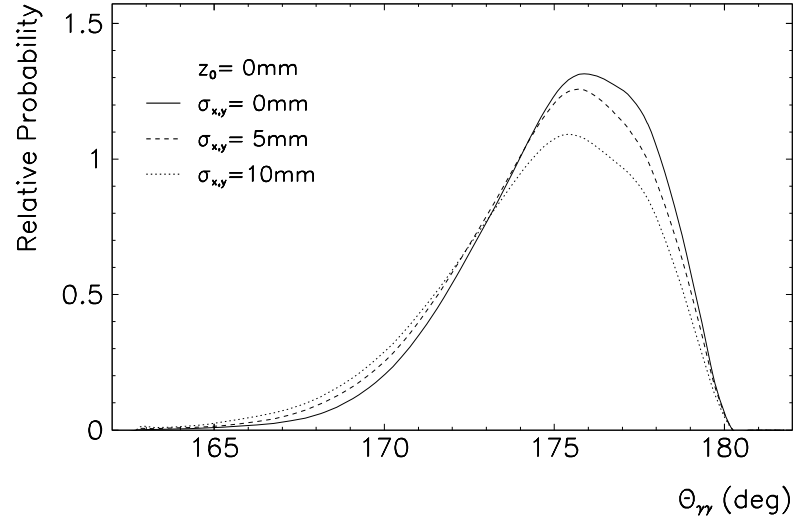


FIGURE 15

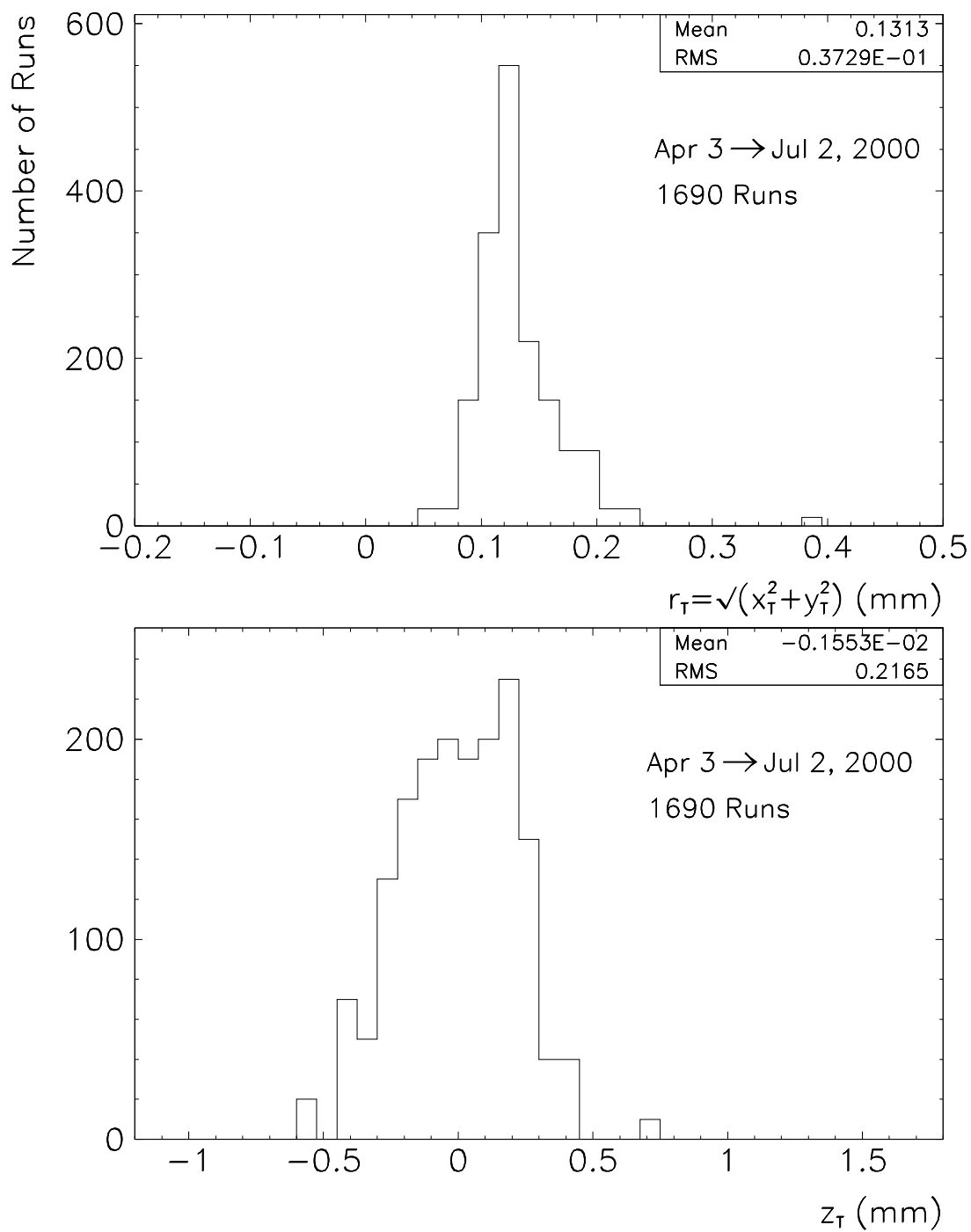


FIGURE 16